

See discussions, stats, and author profiles for this publication at: <https://www.researchgate.net/publication/348753230>

Data-driven Mineral Prospectivity Mapping by Joint Application of Unsupervised Convolutional Auto-encoder Network and Supervised Convolutional Neural Network

Article in Natural Resources Research · January 2021

DOI: 10.1007/s11053-020-09789-y

CITATIONS

8

READS

327

8 authors, including:



Shuai Zhang

China Aero Geophysical Survey and Remote Sensing Center for Natural Resources...

10 PUBLICATIONS 65 CITATIONS

[SEE PROFILE](#)



Emmanuel John M. Carranza

University of KwaZulu-Natal

331 PUBLICATIONS 11,726 CITATIONS

[SEE PROFILE](#)



Hantao Wei

Central South University

20 PUBLICATIONS 99 CITATIONS

[SEE PROFILE](#)



Fan Yang

Lanzhou University

29 PUBLICATIONS 389 CITATIONS

[SEE PROFILE](#)

Some of the authors of this publication are also working on these related projects:



The analysis of the topographic signature of anthropogenic geomorphic processes [View project](#)



Tuff interval in Yangchang Formation of Triassic age in Ordos Basin [View project](#)



Original Paper

Data-driven Mineral Prospectivity Mapping by Joint Application of Unsupervised Convolutional Auto-encoder Network and Supervised Convolutional Neural Network

Shuai Zhang^{1,2,5}, Emmanuel John M. Carranza,^{2,5} Hantao Wei,^{3,5} Keyan Xiao,^{3,5}
Fan Yang,^{1,4} Jie Xiang,³ Shihong Zhang,^{1,3} and Yang Xu^{1,3}

Received 6 September 2020; accepted 4 December 2020

The excellent performance of convolutional neural network (CNN) and its variants in image classification makes it a potential perfect candidate for dealing with multi-geoinformation involving abundant spatial information. In this paper, we tested, for data-driven mineral prospectivity mapping, the efficacy of using unsupervised convolutional auto-encoder network (CAE) to support CNN modeling for synthesis of multi-geoinformation. First, two simple unsupervised CAE networks were constructed to distinguish patches of tif image (i.e., nine predictive evidence maps forming a tif-format image) with nine channels that have high reconstructed errors, which represent prospective areas (i.e., mineralized). Then, the patches of tif image with the lowest reconstructed errors were regarded as background (or non-prospective areas). We varied the CAE network architecture and training epochs and combinations of evidence maps for trials to obtain reliable results. Then, the AUC, or area under the receiver operating characteristic curve, was used to demonstrate empirically that high reconstructed errors are representative of spatial signatures of prospective areas. The proposed coherent spatial signatures, namely patches of a tif image with the highest reconstructed errors and the lowest reconstructed errors representing prospective and non-prospective areas, respectively, were used in the subsequent CNN modeling. The results of CNN modeling using training data derived from CAE exhibited strong spatial correlation with known Au deposits in the study area. The training loss and accuracy of the CNN modeling together with resulting favorability map that were comparable with results from previous study proved the plausibility of the proposed methodology, and therefore, the practice of extracting coherent spatial signatures of prospective and non-prospective areas in unsupervised manner using CAE network and then using these coherent spatial signatures in supervised learning with CNN is a new potential approach for mineral prospectivity mapping.

KEY WORDS: Deep learning, Convolutional neural network, Unsupervised convolutional auto-encoder network, Mineral prospectivity mapping.

¹School of Earth Sciences and Resources, China University of Geosciences Beijing, 29 Xueyuan Road, Beijing 100083, China.

²School of Agricultural, Earth and Environmental Sciences, University of KwaZulu-Natal, Westville Campus, Durban, South Africa.

³MIR Key Laboratory of Metallogeny and Mineral Resource Assessment, Institute of Mineral Resources, Chinese Academy of Geological Sciences, Beijing 100037, China.

⁴Key Laboratory of Mineral Resources in Western China (Gansu Province), School of Earth Sciences, Lanzhou University, Lanzhou 730000, China.

⁵To whom correspondence should be addressed; e-mail: zhshuai@cugb.edu.cn, ejmcarranza@gmail.com, csuwh@126.com, kyanxiao@sohu.com

INTRODUCTION

There are two intrinsic assumptions in mineral prospectivity mapping (MPM) (Carranza 2008). Firstly, particular locations have mineral prospectivity if they are characterized by the same or similar spatial signatures or footprints as known locations where mineral deposits of the type sought exist. Secondly, if more sets of spatial signatures or footprints are present in one location than in another location in a region that is geologically permissive to mineralization, then the former has higher mineral prospectivity than the latter. Therefore, in MPM, either by data- or knowledge-driven approaches, it is necessary to have an assumption of the existence of spatial signatures or footprints of the sought mineralization in the input datasets (Stensgaard et al. 2006).

In data-driven MPM, known deposit-type locations are required to create a training set with tacit assumption that they are coherent (i.e., having strongly similar spatial signatures), which is crucial for training a quantitative model for prediction of exploration targets (or locations) where undiscovered deposits exist. However, mineral deposits, even those of the same type, are unique and show dissimilar characteristics among each other. Hence, multivariate spatial signatures of deposit-type locations are expected to be non-coherent to some extent. This undermines the quality of data-driven MPM output. To address this problem in data-driven MPM, Stensgaard et al. (2006) described a cross-validation statistical procedure for characterizing the spatial signatures of geological features like mineral occurrences. They used likelihood ratio (empirical distribution function for areas with known occurrences versus that for areas without known occurrences) to accentuate the different characteristics of locations with and without mineral occurrences. They then compared and assessed whether the spatial signature of one mineral occurrence can predict the existence of another (presumed to be undiscovered) mineral occurrence in order to evaluate the degree of coherence of spatial signatures of mineral occurrences. In another study, Carranza et al. (2008) proposed a two-step methodology for selecting a training set of deposit-type locations with coherent spatial signatures. The first step involved analysis of mineral favorability scores of univariate geoscience spatial data regarding deposit and non-deposit locations by cumulative

frequency distribution. In the second step, logistic regression was applied to select deposit-type locations with similar multivariate spatial signatures for prospectivity mapping. In this study, the term of mineral occurrence is defined as a concentration of minerals of potential economic interest but has no economic value at present, while the mineral deposit refers to economic concentrations of metals or other mineral commodities (Stensgaard et al. 2006).

For data-driven MPM, many machine learning algorithms have been applied for multi-geoinformation analysis and synthesis (Carranza and Laborte 2015a, b, c; Chen 2015; Rodriguez-Galiano et al. 2015; Chen and Wu 2017; Fatehi and Asadi 2017; Shabankareh and Hezarkhani 2017; Liu et al. 2018; Zhang et al. 2019a). Some scholars have used probabilistic artificial neural networks for MPM (e.g., Leite and Filho 2009) and deep auto-encoder networks for geochemical anomaly mapping (Xiong and Zuo 2016; Moeini and Torab 2017; Xiong et al. 2018; Zhang et al. 2019b). Zuo et al. (2019) reviewed the most popular deep learning algorithms that have been used for geochemical anomaly mapping.

The past decade has witnessed great success in deep learning, which organizes nonlinear modules into multiple layers to transform representation to a higher abstract level (Wason 2018). Such structured learning models can learn complex functions (Le-Cun et al. 2015), and their ability to learn features automatically instead of feature layers designed by humans outperforms counterpart machine learning and AI technologies in various domains (Arel et al. 2010; Chen et al. 2017a, b). Among the vast deep learning approaches, convolutional neural networks (CNNs) are unprecedented successful structures, and one of the most crucial property of structured models is the capacity of feature learning largely provided by convolutional filters (Lecun et al. 1990).

A CNN is a choice of architecture that utilizes spatial relationships for reducing the number of parameters. The intimate relationship between layers and spatial information in CNN architecture makes it a perfect tool for image processing and information extraction (Arel et al. 2010). The high-level performance of CNNs has brought about a variety of convolutional techniques. Tiled convolution (Ngiam et al. 2010) applies different filters with close receptive fields on the inputs. Dilated convolution (Yu and Koltun 2015) expands the receptiveness of a filter without increasing the number of parameters. Network in network (Lin et al. 2013) utilizes micro-network (e.g., multilayer perceptron)

Data-driven Mineral Prospectivity

structure as filters. Inception (Szegedy et al. 2015) whereby a single convolution layer contains filters with different sizes. Common to these CNN variants is the ability to change filters for different applications, implying that convolution is the key element in deep learning architectures. However, the use of CNNs, which has already gained extreme popularity in the field of computer vision, is still at its infancy in the field of MPM or geochemical anomaly mapping. Granek (2016) tested the efficacy of CNN for MPM using a synthetic dataset created with three channels and 500 positive and negative training samples. Nonetheless, Hronsky and Kreuzer (2019) argued that the principal reason for the lack of uptake of MPM within the global mineral exploration industry is not related primarily to the weakness of methodology applied but it is related to input data and to how they are interpreted and used in the process, which limit the effectiveness of MPM. They then proposed a hybrid method that clearly separates input geological interpretation and spatial prospectivity modeling algorithms aiming at integrating the highly refined pattern-recognition skills of human mind and rigorous discipline, objectivity and repeatability of a machine-based algorithm and finally suggested a roadmap toward effective MPM in future.

Despite their great potential applications, machine-based algorithms are not immune to the two most common problems that plague data-driven MPM, namely (1) insufficient training locations with spatially coherent signatures representing known prospective areas and (2) difficulty of selecting training locations representing non-prospective areas. These problems are critical particularly in poorly explored regions with few known mineral deposits (such as the study area, see below).

Sufficiency of training samples (i.e., known mineralized locations) is a key to success in data-driven MPM, whereby relatively balanced deposit (positive) and non-deposit (negative) training datasets are required. However, in reality and in practice, non-mineralized locations largely outnumber known mineralized locations greatly in any study area. This brings about minority positive samples and majority negative samples (Prado et al. 2020). Solutions to such imbalance between minority positive samples and majority negative samples have been proposed at the data level and algorithm level. Data-level solutions comprise over-sampling, under-sampling and their combinations, which are used to increase the number of minority class samples and/or decrease the number of majority class samples to

balance the training datasets before training. At the algorithm level, specific algorithms were improved for correctly classifying the minority class samples (Quinlan 1991; Chawla et al. 2002, 2004; Zadrozny et al. 2003; Jiang et al. 2013). For example, cost-sensitive learning reduces bias toward the majority class samples by assuming higher misclassification cost to minority class samples (Domingos 1999; Elkan 2001; Lu et al. 2003).

Still, some researchers have investigated how to overcome the insufficiency of training samples from the view of MPM. Wang et al. (2020) introduced the semi-supervised random forest to take advantage of the huge of unlabeled data to benefit data-driven MPM, where only few known mineral deposits are available. Li et al. (2020a) asserted that incorporation of CNN and a transfer learning algorithm for identifying highly prospective area can reduce the influence of limited number of known mineral deposits/occurrences; Li et al. (2020b) proposed random-drop data augmentation method for constructing training datasets in the application of CNN for MPM, whereby the proposed data augmentation method adds random noise to MPM data ensuring augmented data remain meaningful in geological sense.

To contribute a novel methodology that also addresses the above-stated problems, it is proposed here to adopt a joint application of algorithms for unsupervised and supervised machine or deep learning. Such joint application of algorithms for unsupervised and supervised learning, generally called semi-supervised learning, which exploits the statistics of unlabeled data (e.g., a mineralized or non-mineralized) to benefit the supervised learning task, is not a new strategy. However, semi-supervised learning has not been demonstrated yet for data-driven MPM, especially in regions with sparse mineral deposits/occurrences like in the study area (see below). Among the most popular machine learning algorithms, both random forest (RF) and support vector machine have semi-supervised learning variant counterparts, which have been used successfully to take advantage of unlabeled data to help improve supervised learning (e.g., Fatehi and Asadi 2017; Wang et al. 2020). Vishnu et al. (2018) applied convolutional auto-encoder (CAE) network for dimensionality reduction, and they used the features in the latent space of CAE as inputs to supervised learning, proving the ability of semi-supervised learning to outperform purely supervised learning in spatial modeling of polymetallic nodule

parameters. Chen et al. (2017a, b) demonstrated semi-supervised deep feature learning for medical image analysis with joint application of CAE (for unsupervised extraction of coherent spatial features from an image with few labeled data) and CNN (for supervised fine tuning and classifier training).

In this paper, inspired by the work of Chen et al. (2017a, b), we explored the potential joint application of CAE network in support of CNN modeling for data-driven MPM. That is, a CAE network was used here for extracting spatially coherent signatures from data features to be used for training a CNN model in order to address the above-mentioned two most common problems that plague data-driven MPM. It is emphasized here that the methodology proposed here does not involve mathematical integration of two distinct mathematical methods/algorithms (i.e., CAE and CNN), rather it is a sequential joint application—first CAE and then CNN—for data-driven MPM. This proposed methodology of using CAE network to support CNN modeling takes advantage of convolution for (a) unsupervised extraction of coherent spatial signatures from input data (by using a CAE network) and (b) supervised synthesis of multi-geoinformation (through CNN modeling) to discriminate between prospective and non-prospective areas.

STUDY AREA AND DATASET

Geology and Mineralization

The study area, the Hezuo–Meiwu district, is dominated by Carboniferous to Triassic marine sedimentary units (Fig. 1). The area is cut by NW–SE trending faults and by the Xiahe–Hezuo regional thrust. The latter structure separates the study area into eastern and western parts with some difference in metallogenetic characteristics.

The eastern part is characterized by Carboniferous to Permian clastic rocks as well as carbonates covering parts of granitoid plutons. These granitoid plutons intruded into the Carboniferous to Permian rocks. The two most prominent granitoid intrusions, Meiwu and Dewulu, occurred in controversial tectonic settings: Jin et al. (2005) favor a subduction setting, whereas Zhang et al. (2007) and Luo et al. (2012a, b) support a post-collision setting. Various dioritic to granodioritic and granitic stocks and dikes in the western part intruded into Triassic marine clastic rocks (Sui et al. 2017a, b).

Only 18 Au deposits/occurrences are presently found in the study area and they show some differences in metallogenetic characteristics. The 12 Au deposits/occurrences comprising the mineralization in the eastern zone, which are dominated by Cu–Au skarn and lode Au deposits, mainly occur in the Dewulu intrusion. The important deposits in or around this intrusion include the Bulagou, Labuzaika, Jili, Laodou and Gangcha lode Au deposits (Jin et al. 2016). The six Au deposits/occurrences comprising the mineralization in the western zone are characterized by disseminated Au hosted mostly in Triassic marine clastic rocks (e.g., Zaozigou and Zaorendao) and less significantly near intermediate to felsic dikes. Although no plutonic bodies are exposed and age and petrogenesis of the magmatic rocks in the western zone are poorly constrained, the magmatism in the western zone, characterized mainly by small stocks and dikes, shows compositional similarity with the plutons in the eastern zone (Jin et al. 2016).

Besides the 18 Au deposits/occurrences, Chen and Gong (2007) reported the existence of seven Cu deposits/occurrences (two of which are small Cu deposits (< 100 kt)) and three Fe deposits/occurrences (one of which is a small Fe deposit (< 100 kt)). The latter are skarn type controlled by strata and magmatic rocks, whereas the former have complex ore genesis controlled by strata (Permian carbonates) or regional intermediate-acid magmatic rocks. In addition,

Despite the apparent differences in geology and mineralization in the eastern and western parts in the study area, geological studies exist that support a connection between these two parts. Firstly, the timing of dikes within and around the Zaozigou gold deposit in the western part is consistent with that of granitoid intrusion in the eastern part (Li et al., 2014). Secondly, hydrothermal sericite ($^{40}\text{Ar}/^{39}\text{Ar}$) dating and C–H–O–S isotope data indicate that the Zaozigou gold deposit was probably precipitated from hydrothermal fluids derived from concealed granitic batholiths (Sui 2012). Thirdly, Jin et al. (2016) argued that, based on geochemical and geochronological data, the Laodou gold deposit in the eastern part most likely precipitated from magmatic-dominated fluids as well. Fourthly, Li et al. (2019a, b) argued that during Early–Middle Triassic, multiple magmatic-hydrothermal gold–polymetallic mineralizing events associated with ilmenite-series intermediate to felsic magmatism took place in the study area, resulting in a reduced intrusion-related

Data-driven Mineral Prospectivity

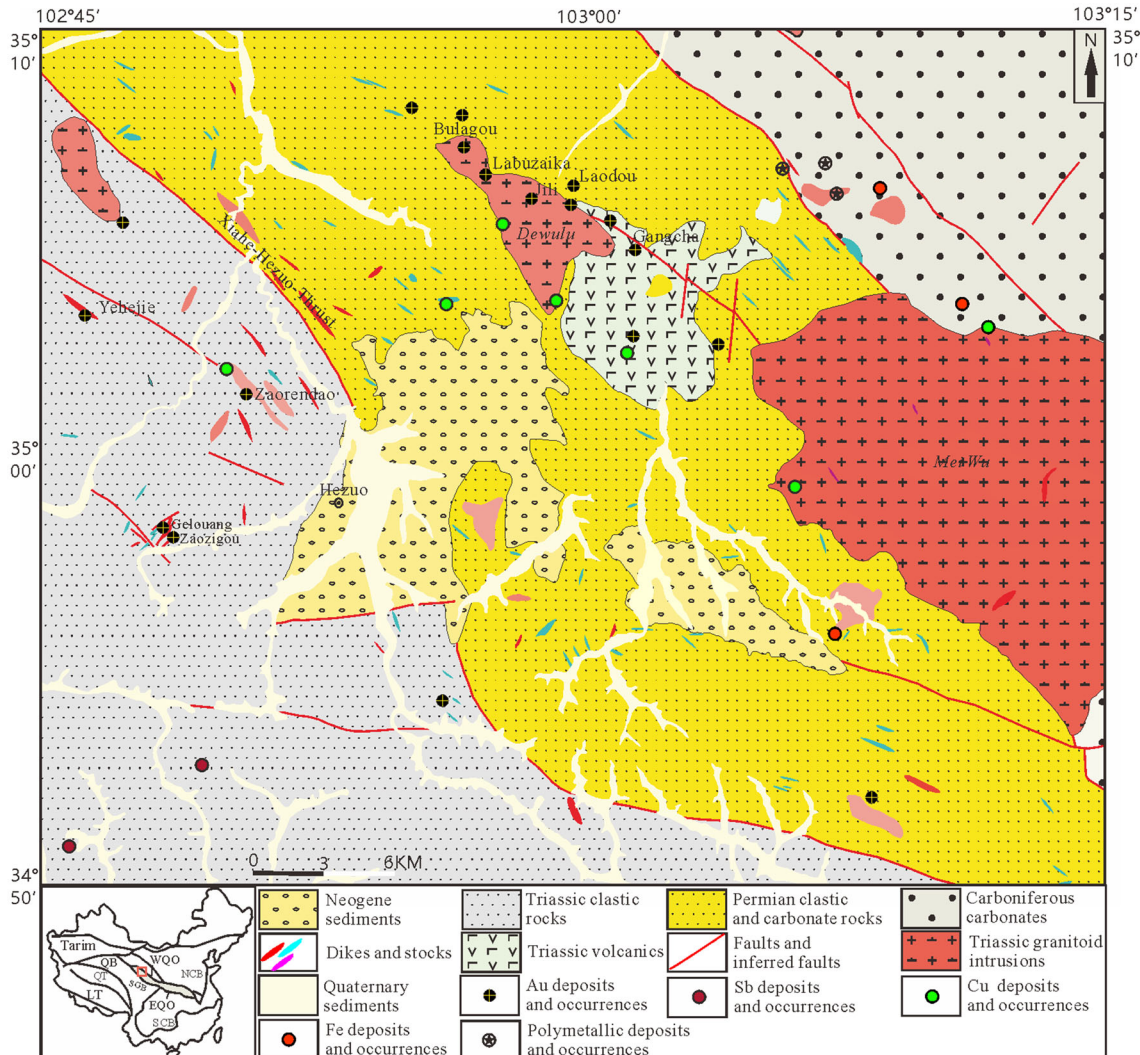


Fig. 1. Geological map of the Hezuo–Meiwu district with sites of major Au deposits modified from Sui et al. 2017a, 2017b.

gold–polymetallic mineral system in the West Qinling Orogen.

Considering that there are different types/styles/commodities of mineral deposits belonging to the same mineral system in the study area, the proposed methodology here for MPM is based on a mineral system approach but not on the traditional mineral deposit model approach. Examples of recent work on mineral system approach to MPM using multi-commodity deposits (i.e., different deposit types/styles belonging to the same mineral system) are discussed in Lindsay et al. (2016) and Occhipinti et al. (2016). These previous works discuss detailed analysis of the mineral system with

multi-commodity deposits in a given study area, which enables the selection of effective evidence maps for MPM.

Dataset

Based on the metallogenetic characteristics of the known gold deposits in the study area, we used nine predictive variables, namely distance to faults and intrusions, singularity indices of Ag, As, Au, Cu, Sb, and PC1 and PC2 from principal components analysis considering the compositional nature of geochemical data. The element data determined from

Table 1. Correlation coefficients of evidence maps

	As	Ag	Au	Cu	Sb	DTF	DTI	PC1	PC2
As	1.00	0.14	0.40	0.25	0.46	0.00	-0.03	0.16	-0.03
Ag	0.14	1.00	0.10	0.17	0.13	0.02	0.02	0.03	-0.06
Au	0.40	0.10	1.00	0.13	0.37	-0.02	-0.04	0.15	0.04
Cu	0.25	0.17	0.13	1.00	0.15	0.01	0.00	0.07	0.04
Sb	0.46	0.13	0.37	0.15	1.00	-0.01	0.08	0.14	-0.04
DTF	0.00	0.02	-0.02	0.01	-0.01	1.00	0.17	0.08	-0.15
DTI	-0.03	0.02	-0.04	0.00	0.08	0.17	1.00	0.10	0.18
PC1	0.16	0.03	0.15	0.07	0.14	0.08	0.10	1.00	-0.04
PC2	-0.03	-0.06	0.04	0.04	-0.04	-0.15	0.18	-0.04	1.00

DTF distance to fault; DTI distance to intrusion; PC1 first principal component; PC2 second principal component

9041 stream sediment samples, which were subjected to singularity and principal components analysis, include those for Au, As, Sb, Hg, Ba, Co, Cu, Pb, Zn, Ag, W and Mo. The samples were collected by the Third Institute of Geology and Mineral Exploration, Gansu Provincial Bureau of Geology and Mineral exploration and Development, Lanzhou, China, at a scale of 1:50,000. For the present study, the nine predictive variables with most of them having low correlation coefficient (Table 1) from our previous study (Zhang et al. 2019a), in which we applied maximum entropy and RF modeling for multi-geoinformation synthesis were used.

METHODOLOGY

The case of sparse known deposits is a critical problem in data-driven MPM. Several previous studies have worked successfully, however, with sparse training deposit locations using different methods of data-driven MPM: 12 porphyry Cu deposits in weights of evidence (WofE) and random forest (Carranza 2004; Carranza and Laborte 2015c), 13 hydrothermal vents in WofE and weighted logistic regression (Agterberg et al. 1993; Agterberg and Cheng 2002), and 19 epithermal Au deposits in WofE, logistic regression and evidential belief function (Carranza and Hale 2001a, 2001b, 2003). Here, only 18 Au deposits are available for data-driven MPM and the proposed methodology, which involves sequential joint application of first CAE (for unsupervised extraction of coherent spatial signatures from input data) and followed by CNN (for supervised synthesis of multi-geoinformation), is a novel attempt to address the problem.

Convolutional Auto-Encoder (CAE)

Auto-encoder network aims to reconstruct input data and compare them with original data. The learning process involves using the reconstructed input data to approximate the original input data by optimizing the values of a cost function. Generally, an auto-encoder network is composed of two parts and a final training by optimization. The standard auto-encoder network is described as follows.

The encoder is described by two functions: $Z = \text{Enc}_z(Y; W_C)$ and $U = \text{Enc}_U(Y; W_C)$, while the decoder function is depicted as $\text{Dec}(Z, U; W_D)$, where Y denotes the input image, W_C and W_D represent the trainable parameter vector of the encoder and decoder, respectively, Z is the invariant feature vector, and U is the transformation parameter vector. Finally, the reconstructed error $E_D = |Y - \text{Dec}(Z, U; W_D)|^2$ measures the Euclidean distance between the input Y and its reconstruction.

The convolutional version of the auto-encoder combines convolutional operation with the auto-encoder structure. This adaptation enables the new CAE structure to utilize the capacity of feature learning provided by convolutional filters and has advantage for coping with spatial-related information in raster images. As in traditional auto-encoder paradigm, the convolution auto-encoder structure has counterpart convolutional encoder and convolutional decoder. However, by inverse convolutional operation in convolutional decoder and by unsupervised greedy training in standard auto-encoder, the parameters in a convolutional auto-encoder can be optimized (Chen et al 2017a, b).

The procedure of convolution conversion from image-like input to output is called convolutional encoder. Then, the output values are reconstructed

Data-driven Mineral Prospectivity

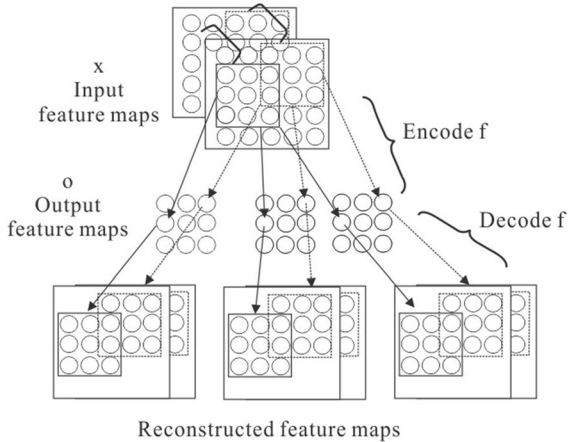


Fig. 2. Unsupervised convolutional auto-encoder network modified from Chen et al. 2017a, 2017b.

through the inverse convolutional operation, which is called convolutional decoder. Moreover, through the standard auto-encoder unsupervised greedy training, the parameters in the encode and decode operations can be calculated.

The convolutional auto-encoder is demonstrated in Figure 2, with input feature maps (usually in the form of image-like matrix) $x \in \mathbb{R}^{n \times l \times 1}$, which are derived from the input layer (where n denotes channels and $l \times l$ represents image size) or a previous layer (where n indicates the number of output feature maps). The number of output feature maps is equivalent to the convolutional kernels at the inner layers of the network and the size of convolutional kernel (d) should not be greater than that of input image 1 ($d \leq l$).

Convolutional Neural Network (CNN)

CNN, proposed by Lecun (Lecun et al. 1990), has become the most powerful tool in the domain of pattern recognition. It can automatically learn hierarchical semantically related representations from input data without any prior knowledge by learning rich contextual information and extending the receptive field (Marmanis et al. 2016). In contrast with traditional handcraft features, high-level representations extracted by CNNs have been proven superior for image classifications (Lu et al. 2017). Generally, a CNN consists of convolutional layers, pooling layers and a full-connected network as well

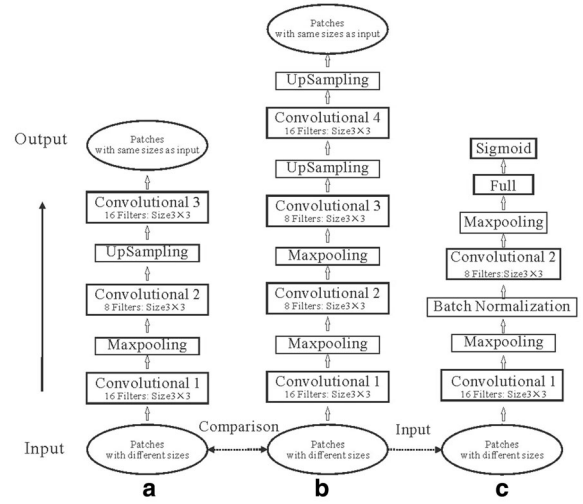


Fig. 3. Architectures of **a**, **b** CAE and **c** CNN. CAE in **a** and **b** are used for comparison with dashed arrow indicating same input. Inputs with the highest and lowest reconstructed errors after CAE **b** serve as inputs to CNN **c** for validation in supervised way. Solid arrow denotes direction of data flow during algorithm training.

as some techniques that have been developed for dealing with its biggest problem, namely over-fitting.

Convolution and Pooling

The convolution process is performed by sliding, over an image, locally trained filters with the same weight and bias, forming a weight sharing mechanism (Ravi et al. 2017). Local receptive field of a neural represents areas that are connected to the previous layers, and the size of the filters determines the scope of the receptive field (Nielsen 2015). The outputs in a convolutional layer can be calculated as in Eq. (1), and the ReLu activation is represented in Eq. (2)

$$x_j^l = f \left(\sum_{i=1, \dots, M} x_i^{l-1} * k_{ij}^l + b_j^l \right), j = 1, \dots, N, \quad (1)$$

$$f(x) = \begin{cases} x & x > 0 \\ 0 & \text{else} \end{cases} \quad (2)$$

where x_j^l indicates the j th outputs, f represents the activation (ReLu or Sigmoid) function, M and N denote the number of feature maps and filters, respectively, x_i^{l-1} is the i th input map, and the k_{ij}^l and

b_j^l represent the j th filters and their corresponding biases.

The pooling process follows the convolution operation and activation, which summarizes the input feature maps. The most popular pooling operations are Max Pooling and Average Pooling. The Average Pooling averages the input values as results, whereas the Max Pooling obtains the maximum values in a convolutional kernel. Generally, the Max Pooling has superior performance than Average Pooling (Li et al. 2019a, b). Through the pooling operation, an image size is largely reduced and visual features can be extracted independently (Sankar et al. 2016).

Fully Connected Layers

The final part of a typical CNN comprises several fully connected (FC) layers, which are essentially backpropagation neural networks (Wu and Zhao 2018) and require input in one-dimension vector fashion. After multiplying the connection weights and the outcomes from a previous FC layer and adding a bias value, the resulting value would then be transferred to the next FC layer after passing through the activation function. The output (fc_1) of the calculation in a FC layer can be depicted as:

$$fc_1 = f \left(b + \sum_{q=1}^M w_{1,q} * o_q \right) \quad (3)$$

where f denotes activation function, w represents weight vector, o is outcome of the q th neuron, b is bias value, and M is number of neurons.

Dropout and Batch Normalization

The term dropout means dropping out units in a neural network by temporarily and randomly removing some units from the network. This method can be generally adopted for graphical models not limited to feed-forward neural nets, which make the learning process more reliable by reducing over-fitting. Additionally, it offers an approach for approximately combining many different neural network architectures efficiently (Srivastava et al. 2014). Apart from dropout, batch normalization normalizes each scalar feature independently by making it have a mean of zero and a variance of 1.

This technique avoids continuous adaptation to varied new distribution caused by changes of parameters in previous layers during training (Ioffe and Szegedy 2015).

Overall Architecture

Here, two simple unsupervised CAE networks are described (Fig. 3a, b) which are first used to derive the reconstructed errors of patches in tif image and compared one another for the reliability of the reconstructed error distribution and indicative of the mineralization. Then, the CNN structure (Fig. 3c) was adopted to support that the spatial signatures represented by reconstructed errors are discriminative and plausible by comparison with previous study. The reasons for the application of these three simple machine learning architectures are threefold. Firstly, to alleviate the difficulty in fabricating a labeled training dataset for training large number of parameters. Secondly, to test the feasibility of convolution modules in extracting useful information from multi-geoinformation for MPM. Thirdly, to test the capacity of dealing with small patches of tif image limited by Max Pooling.

In the unsupervised CAE network, we used the same convolutional layers as in the CNN architecture (Fig. 3c) and removed one Max Pooling and Upsampling to form a simpler CAE architecture for comparison (Fig. 3a). Both of the CAE and CNN architectures are based on Keras (<https://keras.io/>) with parameters such as activation = 'relu,' padding = 'same' and default strides = (1, 1). The CNN model contains four layers with weights. The first two are convolutional and the remaining two are fully connected. Finally, binary cross-entropy loss and 'rmsprop' optimizer are used to compile the overall architecture. Additionally, Max Pooling follows each convolutional layer and the batch normalization and dropout are adopted as well to prevent over-fitting (Fig. 3c).

Model Evaluation

Both CAE and CNN modeling require an image-like multi-dimensional input instead of single vectors. Therefore, for performance evaluation of the joint application of CAE and CNN for MPM, as proposed here, the nine predictive variables used previously by Zhang et al. (2019a), who applied

Data-driven Mineral Prospectivity

maximum entropy and random forest modeling for MPM, were used here as well. Data for the nine predictive variables were pre-processed as respective nine channels in a tif-format image with pixel size of 50×50 m, forming the source dataset for the joint application of CNN and CAE for MPM.

Thus, firstly, training data were extracted as patches of tif image with nine channels that have sizes of 32×32 pixels, 24×24 pixels and 12×12 pixels as input for CAE. The smallest size of image-like training data constrained by unsupervised CAE structure (Fig. 3b) with convolutional filter of 3×3 and two Max Pooling modules with size 2×2 , turned out to be the size of $12(3 \times 2 \times 2) \times 12(3 \times 2 \times 2) \times 9$ (channels). We doubled the image-like input size and selected an arbitrary size of $32 \times 32 \times 9$ for comparing the resulting reconstructed errors. Then, considering that patches of tif image with false high reconstructed errors may not be representative of prospective areas (positive training samples), the area under the receiver operating characteristic curve (AUC-ROC) (Bradley 1997) was utilized to quantify the higher reconstructed errors' representativeness of prospective areas. The AUC-ROC is of great use for visualizing the performance of a classification algorithm as the decision threshold is varied. Therefore, based on AUC-ROC analysis, we used the reconstructed errors derived from CAE modeling as varied decision thresholds to evaluate the representativeness of higher reconstructive errors as measures of mineral prospectivity in the study area.

After the detailed comparison and evaluation of reconstructed errors as representative of prospective areas, different proportions of tif image patches with high and low reconstructed errors were used for training and synthesizing nine predictive variables by CNN modeling to generate probability maps depicting mineral prospectivity. Then, the success rate curve was used to illustrate the spatial relationship of the known Au deposits with the probability values derived by CNN modeling. The success rate curve is an occurrence-area proportion plot depicting proportions of known deposits versus proportions of prospective area determined by cumulative decreasing cutoff probabilities (Agterberg and Bonham-Carter 2005), usually at 5-percentile intervals. The highest probability (100%) corresponds to minimum proportion of prospectivity pixels (i.e., mineralized areas are naturally rare phenomena) and the lowest probability corresponds

to maximum proportion of a study area (i.e., any area is almost wholly non-mineralized).

RESULTS

The joint application of CAE and CNN for distinguishing prospective area and background was performed following the methodology described above, and theory of mineral system (Joly et al. 2015), was adopted to help clarify the resultant probability map. The patches of tif image(at 50 m per pixel) sizes of 32×32 , 24×24 , and 12×12 representing actual areas of 1600×1600 m, 1200×1200 m and 600×600 m, respectively, were fed into the CAE network aiming at making sure the patch size of tif image is suitable for subsequent CNN model.

Results of CAE Modeling

The spatial distributions of high reconstructed errors (red areas in Fig. 4) shows a consistent trend with varied patch sizes of tif image, which imply that CAE is capable of learning meaningful abstract representation for multi-source geoinformation at several scales. To test the stability of the reconstructed errors and to determine how each evidence variable affects the reconstructed errors, we first reduced the one Max Pooling and Upsampling layer (Fig. 3a) and varied the epochs during training. The resulting reconstructed errors using a reduced layer and different epochs have correlations of > 0.91 (Table 2), which means that the reconstructed errors are seldom affected by the change of CAE architectures (Fig. 3a, b) and the training process. Hence, the CAE yielded reliable high and low reconstructed errors as spatial signatures of prospective areas and non-prospective areas, respectively. Then, each evidence variable was removed successively from the nine channels of tif images, resulting in eight channels of tif image (i.e., the remaining eight evidence variables) (Fig. 5). The distributions of reconstructed errors derived from the eight channels of tif images were compared with those of the nine channels of tif images by correlation analysis. The higher correlation coefficients of reconstructed errors derived from the eight channels of tif images imply that the removed evidence has little contribution to the reconstructed errors derived from the nine channels of tif images. Table 3 indicates that

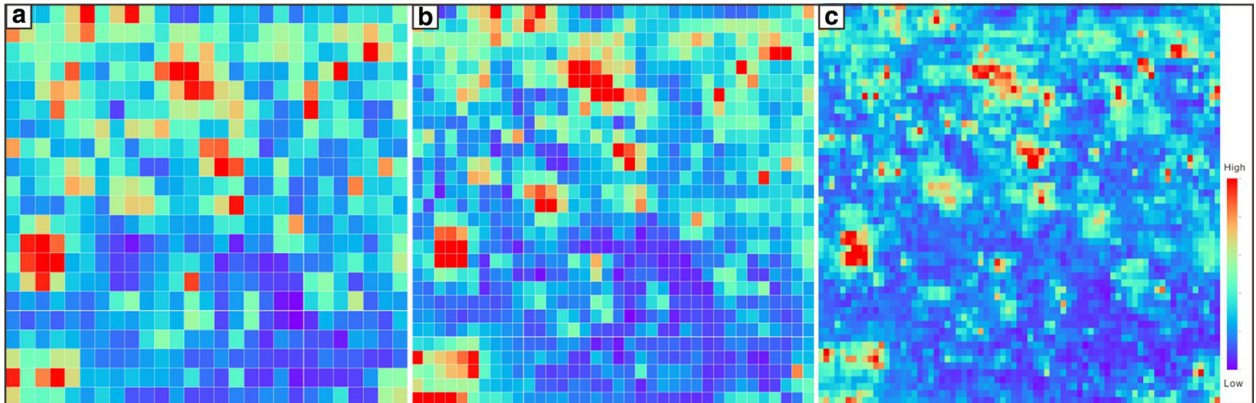


Fig. 4. Reconstructed errors obtained by CAE using different patch sizes of tif image: **a** 32×32 pixels; **b** 24×24 pixels; and **c** 12×12 pixels.

Table 2. Correlation of results from CAE using a reduced layer and different epochs

Correlation	Layer reduction	20 epochs	100 epochs
Layer reduction	1	0.978	0.9108
20 epochs	0.978	1	0.911
100 epochs	0.9108	0.911	1

the evident maps of singularity of Au (0.865), Sb (0.875) and Ag (0.876) contributed most in generating the reconstructed errors, while the evidence maps of PC1 (0.957), singularity map of Cu (0.942) and PC2 have relative less contributions.

Among the resulting reconstructed errors, the CAE classification yielded the highest AUC-ROC (0.853) when using all nine evidence maps for distinguishing spatial signatures of all Au, Fe, Cu, Sb and polymetallic deposits/occurrences (i.e., a total of 33 mineralized locations) in the study area (Fig. 6). This means that all evidence maps contributed to the reconstructed errors to distinguish between spatial signatures of mineralized locations and spatial signatures of non-mineralized locations in the study area. However, the AUC-ROC for the CAE classification for distinguishing spatial signatures of only the 18 Au deposits/occurrences (Fig. 7) is greater than that of the AUC-ROC for the CAE classification for distinguishing spatial signatures of only Fe, Cu, Sb and polymetallic deposits/occurrences (i.e., a total of 15 mineralized locations) (Fig. 8). From this, we deduce that all the evidence variables that were used cater to metallogenetic characteristics of Au de-

posits/occurrences help to diminish partly the false reconstructed errors for prospective areas representative of Au mineralization. The reconstructed errors derived from CAE modeling using evidence variables conceptualized through Au deposit metallogenetic analysis also show strong spatial correlation with the other deposits/occurrences, especially Sb occurrences, in the southwest corner of the study area (Fig. 9). This implies that the other non-Au (i.e., Fe, Cu, Sb and polymetallic) deposits/occurrences in the study area likely belong to the mineral system that formed the Au deposits/occurrences.

Results of CNN Modeling

In the light of the above results from CAE modeling, the smallest size of tif image of 12×12 was considered to contain sufficient information as spatial signatures for distinguishing prospective and non-prospective areas. We then constrained the smallest patch size of tif image to 12×12 for two reasons: (1) the patch size of tif image limits the number of Max Pooling strategy in CAE architecture; and (2) the corresponding actual area of $600 \text{ m} \times 600 \text{ m}$ is comparable to actual lateral extent of individual Au deposits/occurrences in the study area.

To determine what proportions of high and low reconstructed errors would serve best as spatial signatures of prospective and non-prospective areas, respectively, different proportions of tif image patches were obtained from the resulting patches of tif

Data-driven Mineral Prospectivity

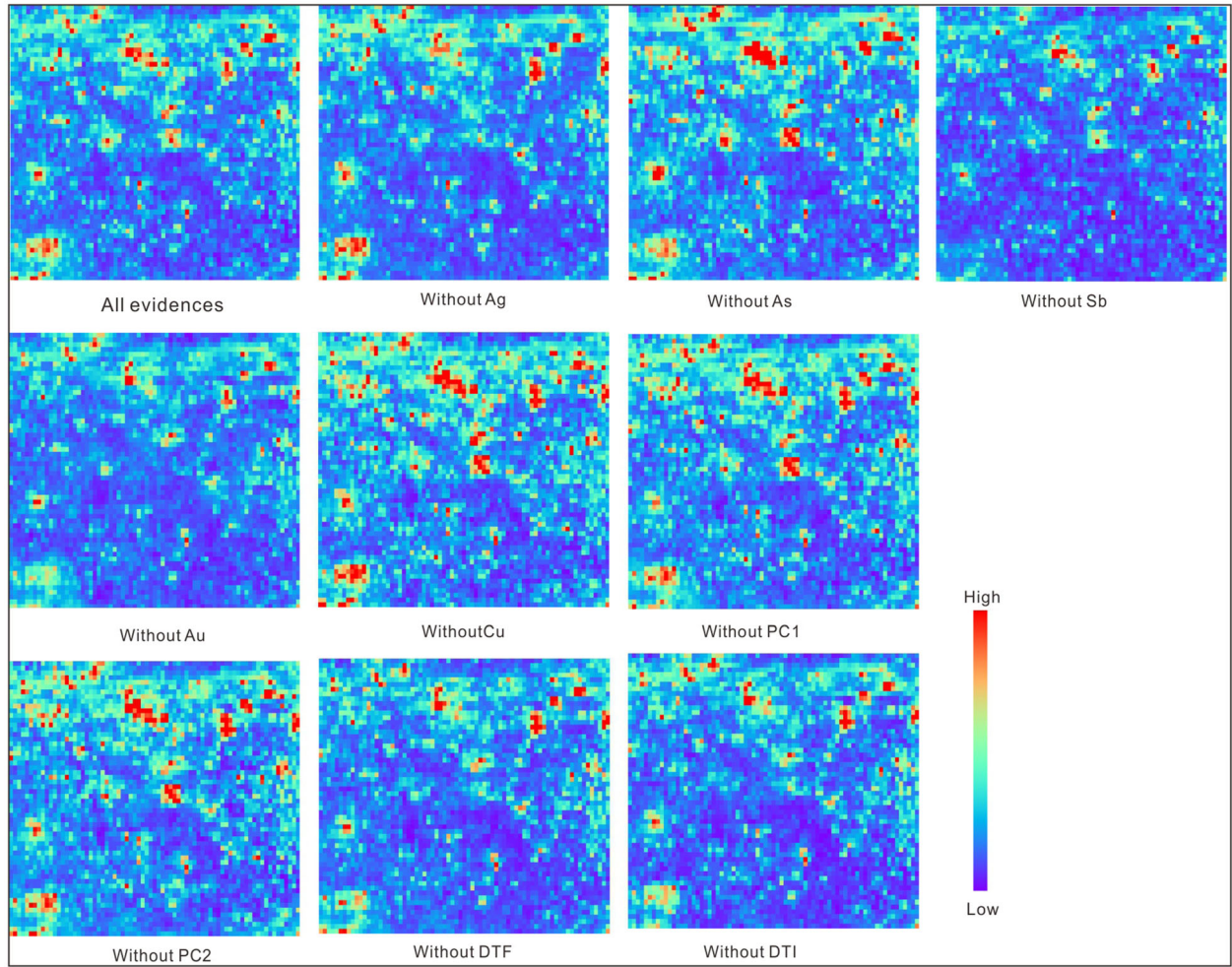


Fig. 5. Reconstructed error with evidence successively excluded in the CAE.

Table 3. Correlation of resulting reconstructed errors with evidence successively excluded

Correlations	Without Sb	Without Cu	Without Au	Without As	Without Ag	Without DTF	Without DTI	Without PC1	Without PC2	All evidence
Without Sb	1.000	0.850	0.827	0.841	0.760	0.855	0.862	0.876	0.865	0.875
Without Cu	0.850	1.000	0.817	0.880	0.814	0.848	0.858	0.949	0.937	0.942
Without Au	0.827	0.817	1.000	0.782	0.839	0.940	0.939	0.830	0.817	0.865
Without As	0.841	0.880	0.782	1.000	0.760	0.786	0.809	0.899	0.897	0.909
Without Ag	0.760	0.814	0.839	0.760	1.000	0.882	0.898	0.841	0.863	0.876
Without DTF	0.855	0.848	0.940	0.786	0.882	1.000	0.959	0.883	0.885	0.890
Without DTI	0.862	0.858	0.939	0.809	0.898	0.959	1.000	0.893	0.890	0.907
Without PC1	0.876	0.949	0.830	0.899	0.841	0.883	0.893	1.000	0.977	0.957
Without PC2	0.865	0.937	0.817	0.897	0.863	0.885	0.890	0.977	1.000	0.932
All evidence	0.875	0.942	0.865	0.909	0.876	0.890	0.907	0.957	0.932	1.000

DTF distance to fault; DTI distance to intrusive; Without Sb without singularity Sb evidence variable, etc.

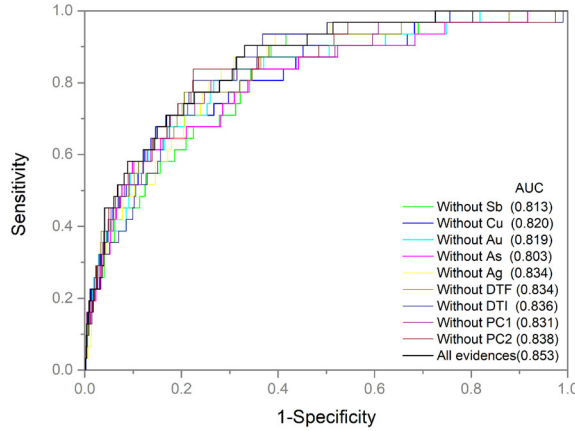


Fig. 6. ROC curves for CAE in discriminating all Au, Fe, Cu, Sb and polymetallic deposits/occurrences in the study area (DTF: distance to fault; DTI: distance to intrusive; Without Sb: without singularity Sb evidence variable, etc.).

image (a totally 4234 patches of tif image) for reducing uncertainties to some extent in training samples. Four labeled training datasets were generated, namely (1) 10% of high reconstructed errors and 10% low reconstructed errors, (2) 15% of high reconstructed errors and 15% low reconstructed errors, and (3) 10% of high reconstructed errors and 30% low reconstructed errors. (4) 50% of high reconstructed errors and 50% low reconstructed errors. Traditional regression models are optimal when the number of positive samples (e.g., mineralized locations) is equal to that of negative samples (e.g., non-mineralized locations) (Breslow and Cain 1988), and our previous study indicated that 19% of study area contains $> 88\%$ of the known deposits (Zhang et al. 2019a). The reasons for creating the third training dataset are twofold. Firstly, the nature of mineralization as a rare phenomenon and that non-mineralized locations account for much larger proportion of any area. Secondly, a relatively larger training dataset compared to other two datasets may increase information during training for background recognition. Besides the three training datasets, the fourth training dataset was created mainly to provide comparison by using 50–50 proportions of high and low reconstructed errors for training the CNN.

In training the CNN model, the training loss gradually dropped to 0.1, while the training accuracy increased to > 0.95 (Fig. 10). This is satisfactory because the quick convergence of training accuracy and training loss implies that reconstructed errors, derived from evidence maps through CAE modeling, as spatial signatures of prospective and non-

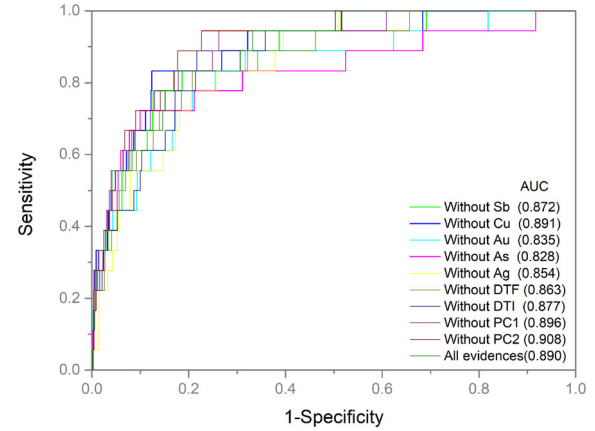


Fig. 7. ROC curves for CAE in discriminating only the 18 Au deposits/occurrences (DTF: distance to fault; DTI: distance to intrusive; Without Sb: without singularity Sb evidence variable, etc.).

prospective areas do exist and are feasible for training of supervised CNN. With the fourth training dataset, the prediction map distinguishes weakly between prospective and non-prospective areas (Fig. 11d), but it has ideal training loss and training accuracy (Fig. 10d). From this, we deduced that there are certain proportions of reconstructed errors that serve well as spatial signatures of prospective and non-prospective areas.

The prediction maps produced by CAE-supported CNN modeling with the first three generated training datasets exhibit visually similar mineralization trends (Fig. 11a–c). After many trials, the second training dataset with 15% high reconstructed errors and 15% low reconstructed errors yielded the best prediction map because it has high probabilities that coincide with most of the known Au deposits/occurrences, and so we subjected this map to further quantitative comparison of performance (Fig. 11b). The success rate curve for this map shows that the predicted potentially mineralized areas occupy 23.8% of the study area and contain 77.8% of the known Au deposits/occurrences (Fig. 12a). The newly delineated potentially mineralized area (~ 200 patches in the tif image) in the northeast and southwest corners of the study area, which account for 4.7% of the study area, provide the difference from MPM using MaxEntropy or RF (19% of study area and containing $> 88\%$ of the known deposits) in our previous study (Zhang et al. 2019a).

When using not only the Au deposits/occurrences but also the Sb, Fe and Cu deposits/occur-

Data-driven Mineral Prospectivity

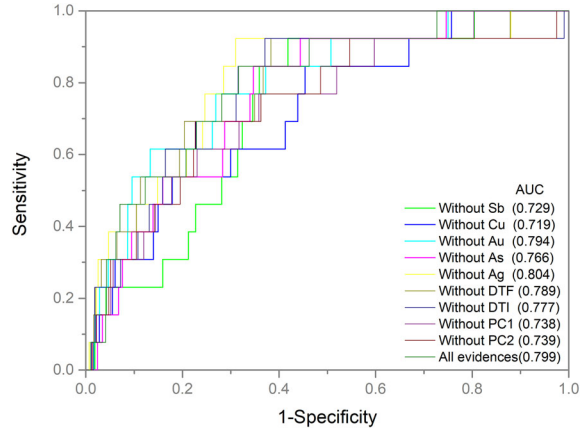


Fig. 8. ROC curves for CAE in discriminating only Fe, Cu, Sb and polymetallic deposits/occurrences (DTF: distance to fault; DTI: distance to intrusive; Without Sb: without singularity Sb evidence variable, etc.).

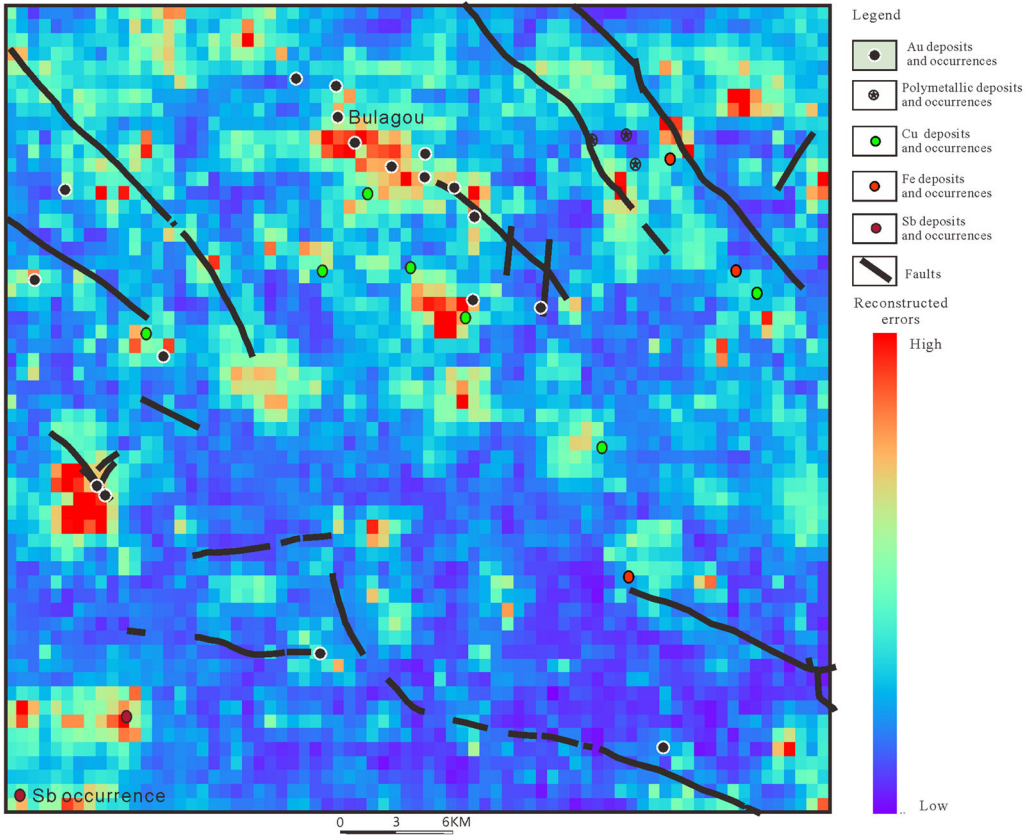


Fig. 9. Reconstructed errors from CAE with patch size of 12×12 pixels.

rences to evaluate the best prediction map in this study (i.e., Fig. 11b) and the best prediction maps in our previous study, all of the five methods exhibit more or less similar performances (Fig. 12b, c). These comparisons have the following significant.

Firstly, with respect to only the known Au deposits/occurrences (Fig. 12a), the other prediction models in our previous study (Zhang et al. 2019a) apparently have better performance of compared to the performance of the CAE-supported CNN model

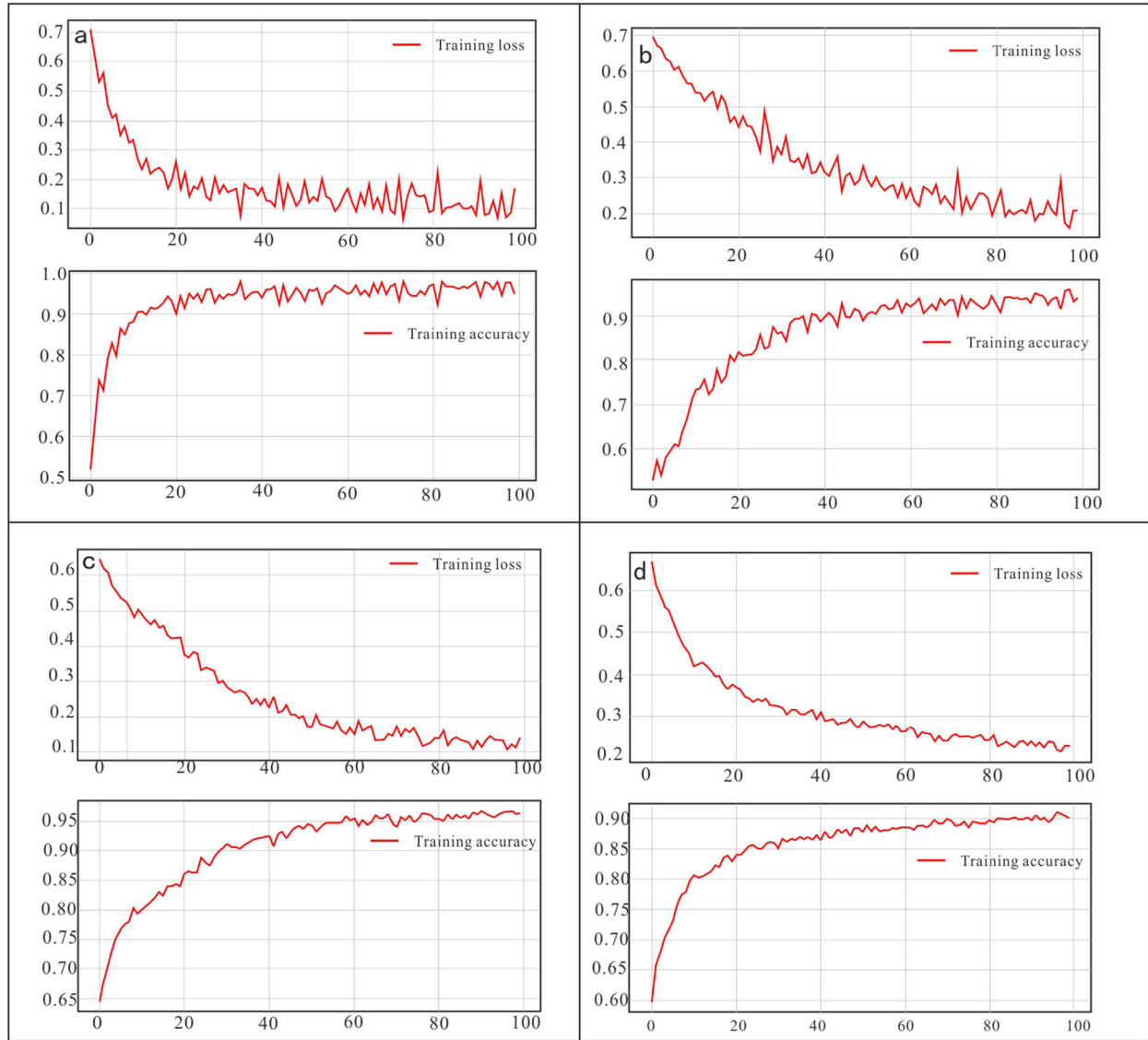


Fig. 10. Training loss and training accuracy of CNNs per training dataset: **a** 10% high reconstructed errors and 10% low reconstructed errors; **b** 15% high reconstructed errors and 15% low reconstructed errors; **c** 10% high reconstructed errors and 30% low reconstructed errors; **d** 50% of high reconstructed errors and 50% low reconstructed errors.

proposed here. This implies that the former models are more strongly capable of recognizing spatial signatures of the main deposit type of interest. Secondly, with respect to the Au and Sb deposits/occurrences (Fig. 12b), the CAE-supported CNN model proposed here has increased performance, whereas the other prediction models in our previous study have reduced performance; this is indicated by comparing Fig. 12b with Fig. 12a. This implies that the CAE-supported CNN model proposed here is

more strongly capable of recognizing spatial signatures of other deposit types that are associated with the main deposit type of interest in the study area. This implies further that the geochemical anomalies detected by the CAE-supported CNN model at the southwest corner of the area (Fig. 11b), which coincide spatially with two Sb occurrences, are not false-positive anomalies. This is because the delineated geochemical anomalies not coinciding with known Au deposits/occurrences coincide with asso-

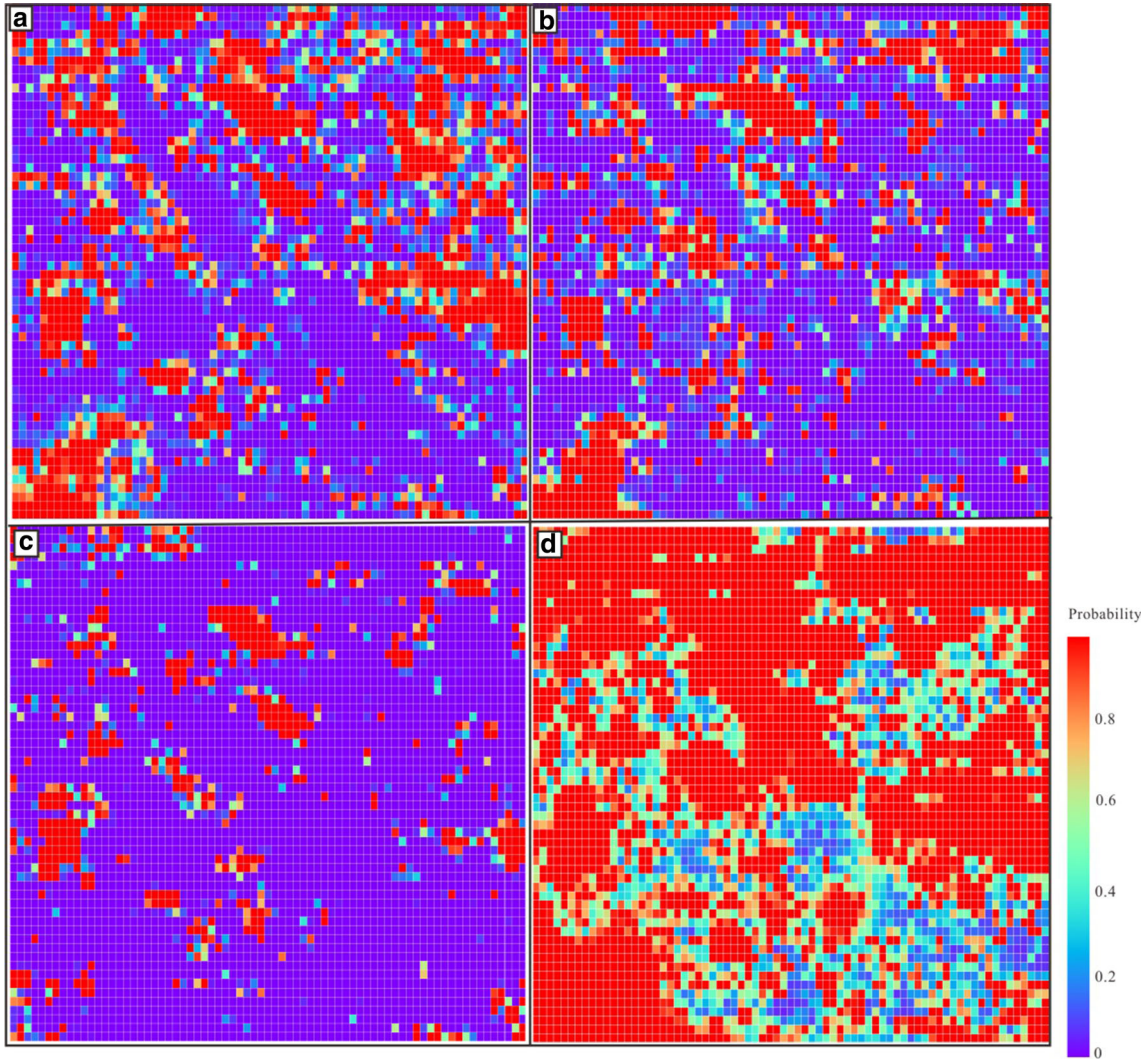


Fig. 11. Prediction maps of CNNs per training dataset: **a** 10% high reconstructed errors and 10% low reconstructed errors; **b** 15% of high reconstructed errors and 15% low reconstructed errors; **c** 10% of high reconstructed errors and 30% low reconstructed errors; **d** 50% of high reconstructed errors and 50% low reconstructed errors.

ciated deposit/occurrences in the same mineral system. Thirdly, with respect to the Au, Sb, Fe and Cu deposits/occurrences (Fig. 12c), the CAE-supported CNN model proposed here has similar performance as the other prediction models in our previous study in recognizing spatial signatures of other deposit types that are associated with the main deposit type of interest in the study area. Our interpretations of the performance evaluations depicted in Figs. 12b and c follow the conclusion of Li et al. (2013) that mineral deposits/occurrences in the study area are products of a reduced intrusion-related gold–poly-metallic mineral system in the West Qinling Orogen.

The distribution of high probabilities in the resulting best prediction map in this study shows consistency with the regional Xiahe–Hezuo faults. All the six Au deposits/occurrences in the western part and eight of the 12 Au deposits/occurrences in the eastern part coincide with high probability in the prediction map of CNN modeling (Fig. 13). Compared with the prediction maps derived by RF and maximum entropy modeling in our previous study (Zhang et al. 2019a), the best prediction map obtained in this present study show higher probabilities in the northeast and southwest corners of the study area (Fig. 13). The interpretation of these high probability areas is as follows:

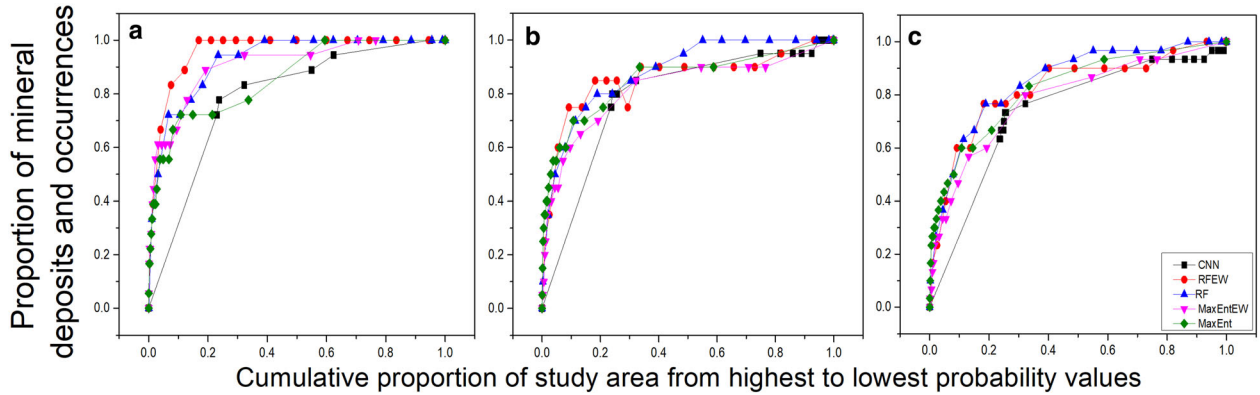


Fig. 12. Success rate curves for CNN model shown in Fig. 11b (i.e., trained with 15% of high reconstructed errors and 15% low reconstructed errors) and for other models, using as testing data: **a** only Au deposits/occurrences; **b** only Au and Sb deposits/occurrences; and **c** all Au, Sb, Fe and Cu deposits/occurrences. Abbreviations: RF = random forest modeling; RFEW = random forest modeling by zones; MaxEnt = maximum entropy modeling; MaxEnEW = maximum entropy modeling by zones and different types of mineral deposits/occurrences. Data for the other models are from Zhang et al. (2019a).

The intrusions became progressively older from the east to the west, which indicate, and is due to, the westward closure of Paleo-Tethyan ocean and a scissor-like collision between the Yangtze and North China cratons (Dong et al. 2012; Luo et al. 2012a, b; Li et al. 2013). Radiometric ages of several granitic dikes in the Zaozigou area are contemporaneous with plutons in the eastern part, implying the same tectonic conditions of intrusion (Sui 2012). Moreover, the group of Cu–Au skarn deposits and intrusion-related Au-vein deposits occurred at a deeper level in the eastern zone, whereas the sediment-hosted Au deposits (e.g., Zaozigou) occurred at a shallower level in the western zone. Their similar ages and origins suggest potential for gold deposit occurrence beneath the sediment-hosted, disseminated gold deposits in the western zone. Disseminated gold deposits in the western zone, corresponding to those in the eastern zone, may have been eroded already (Jin et al. 2016). There are some Sb, Fe and polymetallic deposits/occurrences in and near the newly recognized likely mineralized areas in the northeast and southwest corners of the study area (Fig. 13). For example, there is a Au occurrence just outside the study area located ~11 km north of the Bulagou deposit hosted by the same Carboniferous carbonates underlying the northeast corner. Likewise, there is a Au occurrence located 13.5 km south of the Sb occurrence hosted by the same Triassic clastic rocks in the southwest corner. Moreover, in and near other newly recognized prospective areas, there are also mineral deposits/occurrences. For example, the area slightly westward

from the north is indicated to have high probability. Referring to a 1:250,000 scale geological map of the study area, this predicted prospective area is dominated by Permian clastic and carbonate rocks between two regional faults. There are intrusions (~3 km) and a Au deposit (~3 km) in the periphery area north of the boundary of this predicted prospective area at map scale of 1:250,000 and there are some dikes in the geological map (Fig. 1) of the study area. These features altogether indicate prospectivity for deposits/occurrences of the same mineral system there.

DISCUSSION

The excellent performance of deep learning algorithms in classification especially the CNN is one of our motivations to explore their application in the field of MPM. The CAE results itself indeed can be used unsupervised MPM (Figs. 6, 7, 8); however, the purpose of CAE in the case study was to address the problem of insufficient/sparse training locations for data-driven MPM. The application of CNN in this paper can: a) integrate multiple evidence maps with training dataset derived from CAE; b) inspect the spatial signature of CAE results that used as training dataset, just like traditional data-driven MPM, where known mineralized locations are used to train an algorithm for MPM. To this end, the CAE is the premise to form training dataset as input for CNN in the proposed methodology. CAE and CNN can be tested separately in another data with sufficient

Data-driven Mineral Prospectivity

training locations to compare the feasibility of using CAE for unsupervised MPM by comparing it with supervised MPM using CNN.

Since mineralization is a rare phenomenon or event (Zuo et al. 2019), the scarcity of ground truth and sample of known deposits compared to non-mineralized locations makes supervised deep learning architecture fail to model accurately the complex relationship between predictive variables (i.e., evidence maps) and target variable (i.e., known mineralized locations and randomly selected non-mineralized locations). Furthermore, the target variable varies from mineralization trace to typical deposits and this brings about uncertainty in representing mineralization, let alone randomly selected non-mineralized locations that represent background. In the application of CAE network for

detection of geochemical anomalies, the obtained high reconstructed errors can represent prospective areas, whereas low reconstructed errors indicate background (Xiong and Zuo 2016). Hence, the patches of tif image with high reconstructed errors obtained here by CAE depict spatial signatures similar to or coherent with those at positive training samples (i.e., equivalent to mineralized locations in traditional data-driven MPM), whereas patches of tif image with low reconstructed errors depict spatial signature of background (i.e., non-mineralized) locations. The existence of such spatial signatures is proven by the resulting reliable reconstructed errors and the process of synthesizing multi-geoinformation by CNN modeling.

The proposed methodology based on CAE-derived reconstructed errors can be regarded as an

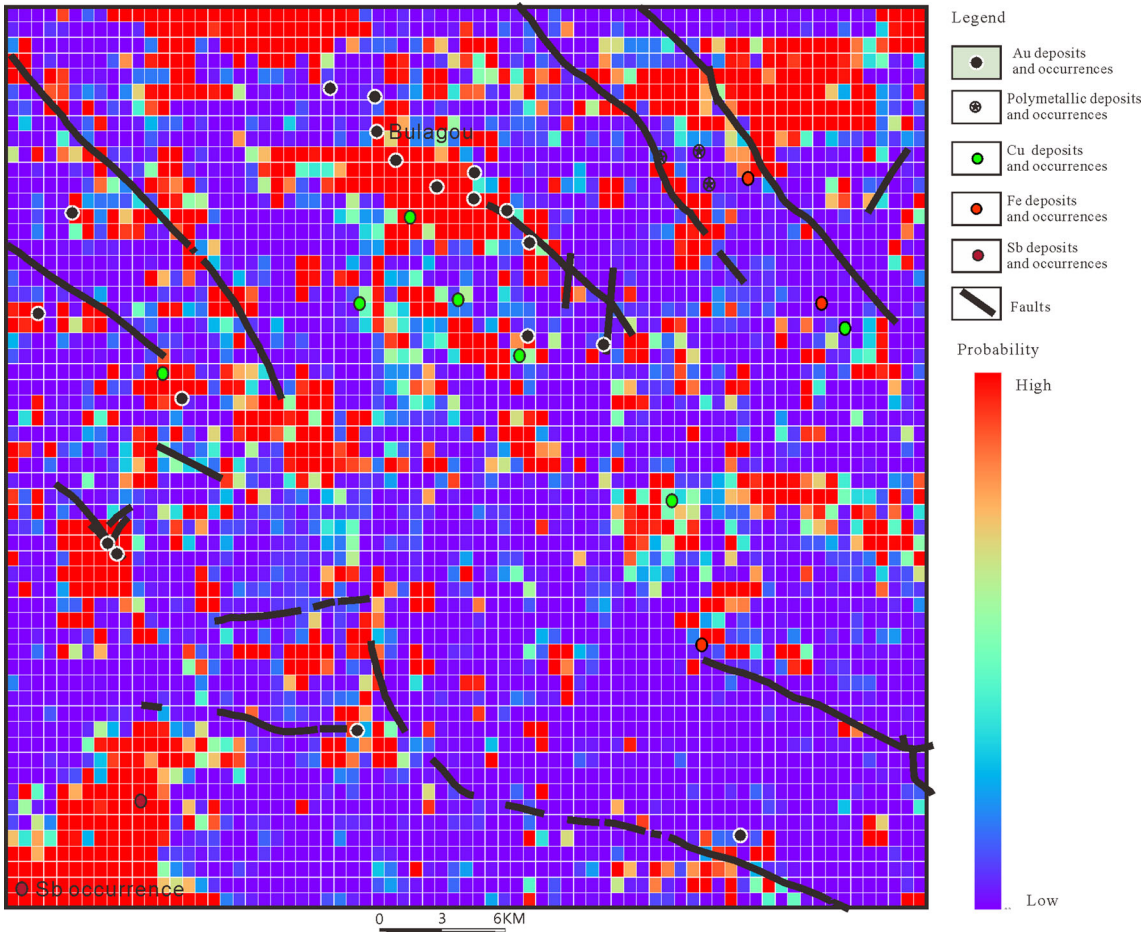


Fig. 13. Prediction map of CNNs (trained with 15% high reconstructed errors and 15% low reconstructed errors) overlain with faults and Au deposits/occurrences.

other fashion of MPM. Just like traditional fashion of MPM, the proposed methodology has an implicit assumption that predicted areas depict spatial signatures similar to those of known mineralized locations (Prado et al. 2020). Searching for meaningful spatial signatures or their proxy is the practical foundation of various methods of MPM. Hence, the use of coherent spatial signatures of mineralized locations determines the accurate performance of supervised MPM. However, the known mineralized locations are not the ones where such spatial signatures are present. Stensgaard et al. (2006), for example, divided their study area into sub-areas with mineralized locations and sub-areas without mineralized locations, and they demonstrated that data values in sub-areas with known mineralized locations are significantly different from those in the sub-areas without mineralized locations (Chung and Keating 2002). Then, based on the empirical distributions of data in the two sub-areas, they generated mineral prospectivity map. However, in addition to the known mineralized locations, they also used locations surrounding the known mineralized locations to help find effective spatial signature of prospective areas. Therefore, this augmentation of positive training samples performed by Stensgaard et al. (2006) is similar to what we performed here through CAE modeling. However, no one knows the optimum number of data values around known mineralized locations that should be used and no one knows the optimum similarity level for choosing data values to depict the spatial signature of prospective areas. Therefore, augmentation of positive training samples through unsupervised CAE modeling is more robust than the augmentation technique of Stensgaard et al. (2006).

Although augmentation of positive training samples through unsupervised CAE modeling shows promising spatial signature in discriminating prospective area in supervised CNN modeling, uncertainty that exists in those CAE-derived patches requires further study. To verify the coherence of spatial signature among training datasets, a simple method can be applied to explore the mutual prediction ability of those selected patches as positive or negative samples. This was demonstrated in MPM carried out by Stensgaard et al. (2006), who used randomly selected mineralized locations to predict other mineralized locations for testing whether a group of mineralized locations have same spatial signature or not. Therefore, it is viable to use one or more patches with high reconstructed errors (i.e.,

outliers in a dataset) to form a training dataset to predict other patches with high reconstructed errors. The supervised learning algorithm is not only effective for integrating multiple evidence maps with CAE-derived patches, but it is also a potential way to inspect the spatial signature among training dataset in the proposed methodology. In addition, using potential maps from data-driven MPM (e.g., WofE) is alternative way for creating training sample, but they need sufficient training locations, which is the problem being addressed in this study. Therefore, such practice leads to circular reasoning that should be avoided in science. Moreover, in all the three scenarios, the CNN model appears to be inferior to other traditional methods of data-driven MPM (Fig. 12). One important reason for this is that MPM is biased toward mature well-known areas (Hronsky et al. 2019), which are often used as locations for selecting training samples and performance evaluation (e.g., ROC). On the other hand, probability of prediction maps from CNN tend to be close to 1 for prospective area and 0 for non-prospective area so the intervals of CNN curve are different from those of other curves (5-percentile intervals). Further investigation on the differences of spatial signature (incoherence of spatial signature) among mineralized locations covered/excluded by CAE-derived patches with high reconstructed errors and their performance in data-driven MPM provides insights into such bias mentioned above. In addition, the training data obtained by CAE were derived in an unsupervised way (i.e., independent of known deposit locations); therefore, an independent test dataset is not needed for evaluating the prediction and modeling uncertainty.

From viewpoint of mineral system, Joly et al. (2015) reported that diverse deposit types might share common metal sources and active fluid pathways, leading to similar prospectivity on the scale of a geological region. Multiple mineral systems may use the same architecture at different times and repeated episodes of mineralization may use the same fluid pathways but different traps and sources; hence, diverse deposits types can occur at the same architecture system. Thus, the reconstructed errors derived by CAE modeling from the same evidence maps that we used in our previous study (Zhang et al. 2019a) may, in fact, depict spatial signatures of deposits/occurrences with various mineralization styles but belonging to a single mineral system in the study area and not just depict spatial signatures of the Au deposits/occurrences. The values of AUC-

Data-driven Mineral Prospectivity

ROC for CAE modeling of spatial signatures of mineralized and non-mineralized locations show that the derived reconstructed errors are indicative of not only the Au deposits/occurrences but of the various types of deposits/occurrences in the study area (Figs. 6, 7, 8). This implies that the theory of mineral system justifies the efficacy of spatial signatures derived from unsupervised learning for distinguishing between prospective and non-prospective areas.

CONCLUSIONS

In the past decade, deep learning has drawn lots of attention and the major challenges in applying the unprecedented successful approaches in other fields to the MPM, same as in traditional machine learning methods are insufficient mineralized locations with coherent spatial signatures as training locations and difficulty of selecting training locations that represent the non-prospective area. The proposed methodology of using CAE to support CNN modeling proves to be effective in MPM by first using unsupervised CAE to augment training dataset and then synthesizing the multi-geoinformation with CNN modeling.

Various measurements (correlation analysis for resulting reconstructed errors, AUC-ROC values, and training loss and accuracy of CNN modeling) verified the reliability and effectiveness of the reconstructed errors from the CAE as spatial signatures of prospective and non-prospective area. The CAE-supported CNN model tends to be more capable of recognizing spatial signatures of mineral deposits/occurrences that belong to a single mineral system in contrast with traditional machine learning algorithms, which are more capable of recognizing spatial signatures of deposits of the type sought.

In contrast with traditional methods or methodologies of data-driven MPM, the methodology of data-driven MPM proposed here suggests to first search for, by unsupervised learning (here by CAE modeling), coherent spatial signatures of prospective and non-prospective areas. Then, these coherent spatial signatures of prospective and non-prospective areas are used further used as training data to synthesize multi-geoinformation, by supervised learning (here by CNN modeling). Finally, the output MPM model is validated using the known mineral deposits/occurrences.

ACKNOWLEDGMENTS

Funding support for this research was derived from the National Key Research and Development Program of China (Project No. 2017YFC0601501), The China National Mineral Resources Assessment Initiative (Project Nos. 1212010733806 and 1,212,011,120,140) and China Scholarship Council (CSC No. 201906400022).

REFERENCES

- Agterberg, F. P., & Bonham-Carter, G. F. (2005). Measuring the performance of mineral-potential maps. *Natural Resources Research*, 14(1), 1–17.
- Agterberg, F. P., & Cheng, Q. (2002). Conditional independence test for weights-of-evidence modeling. *Natural Resources Research*, 11(4), 249–255.
- Agterberg, F. P., Bonham-Carter, G. F., Cheng, Q. M., & Wright, D. F. (1993). Weights of evidence modeling and weighted logistic regression for mineral potential mapping. *Computers in geology*, 25, 13–32.
- Arel, I., Rose, D. C., & Karnowski, T. P. (2010). Deep machine learning - a new frontier in artificial intelligence research [research frontier]. *Computational Intelligence Magazine IEEE*, 5(4), 13–18.
- Bradley, A. P. (1997). The use of the area under the ROC curve in the evaluation of machine learning algorithms. *Pattern recognition*, 30(7), 1145–1159.
- Breslow, N. E., & Cain, K. C. (1988). Logistic regression for two-stage case-control data. *Biometrika*, 75(1), 11–20.
- Carranza, E. J. M. (2004). Weights of evidence modeling of mineral potential, a case study using small number of prospects, Abra. *Philippines. Natural Resources Research*, 13(3), 173–187.
- Carranza, E. J. M. (2008). *Geochemical anomaly and mineral prospectivity mapping in GIS*. Newyork: Elsevier.
- Carranza, E. J. M., & Hale, M. (2001a). Geologically constrained fuzzy mapping of gold mineralization potential, Baguio district. *Philippines. Natural Resources Research*, 10(2), 125–136.
- Carranza, E. J. M., & Hale, M. (2001b). Logistic regression for geologically constrained mapping of gold potential, Baguio district. *Philippines. Exploration and Mining Geology*, 10(3), 165–175.
- Carranza, E. J. M., & Hale, M. (2003). Evidential belief functions for data-driven geologically constrained mapping of gold potential, Baguio district. *Philippines. Ore Geology Reviews*, 22(1–2), 117–132.
- Carranza, E. J. M., & Laborte, A. G. (2015a). Data-driven predictive mapping of gold prospectivity, Baguio district, Philippines, application of random forests algorithm. *Ore Geology Reviews*, 71, 777–787.
- Carranza, E. J. M., & Laborte, A. G. (2015b). Data-driven predictive modeling of mineral prospectivity using random forests, a case study in Catanduanes Island (Philippines). *Natural Resources Research*, 25(1), 1–16.
- Carranza, E. J. M., & Laborte, A. G. (2015c). Random forest predictive modeling of mineral prospectivity with small number of prospects and data with missing values in Abra (Philippines). *Computers & Geosciences*, 74, 60–70.
- Carranza, E. J. M., Hale, M., & Faassen, C. (2008). Selection of coherent deposit-type locations and their application in data-

- driven mineral prospectivity mapping. *Ore Geology Reviews*, 33(3–4), 536–558.
- Chawla, N. V., Bowyer, K. W., Hall, L. O., & Kegelmeyer, W. P. (2002). SMOTE, synthetic minority over-sampling technique. *Journal of artificial intelligence research*, 16, 321–357.
- Chawla, N. V., Japkowicz, N., & Kotcz, A. (2004). Special issue on learning from imbalanced data sets. *ACM SIGKDD explorations newsletter*, 6(1), 1–6.
- Chen, M., Shi, X., Zhang, Y., Wu, D., & Guizani, M. (2017a). Deep features learning for medical image analysis with convolutional autoencoder neural network. *IEEE Transactions on Big Data*. <https://doi.org/10.1109/TBDA.2017.2717439>.
- Chen, T., Xu, R., He, Y., & Wang, X. (2017b). Improving sentiment analysis via sentence type classification using BiLSTM-CRF and CNN. *Expert Systems with Applications*, 72, 221–230.
- Chen, Y., & Y., & Gong, Q, S. . (2007). Discussion on the division of deposit scale and the index of ore prospecting. *GANSU GEOLOGY*, 16(3), 6–11. (**In Chinese**).
- Chen, Y. (2015). Mineral potential mapping with a restricted Boltzmann machine. *Ore Geology Reviews*, 71, 749–760.
- Chen, Y., & Wu, W. (2017). Mapping mineral prospectivity using an extreme learning machine regression. *Ore Geology Reviews*, 80, 200–213.
- Chung, C. J., & Keating, P. B. (2002). Mineral potential evaluation based on airborne geophysical data. *Exploration Geophysics*, 33(1), 28–34.
- Domingos, P. (1999). *A general method for making classifiers cost-sensitive* (pp. 1049–1001). Instituto Superior Técnico, Lisboa: Artificial Intelligence Group.
- Dong, Y., Liu, X., Zhang, G., Chen, Q., Zhang, X., Li, W., et al. (2012). Triassic diorites and granitoids in the Foping area, constraints on the conversion from subduction to collision in the Qinling orogen, China. *Journal of Asian Earth Sciences*, 47, 123–142.
- Elkan, C. (2001). The foundations of cost-sensitive learning. Paper presented at the International joint conference on artificial intelligence.
- Fatehi, M., & Asadi, H. H. (2017). Data integration modeling applied to drill hole planning through semi-supervised learning, a case study from the Dalli Cu-Au porphyry deposit in the central Iran. *Journal of African Earth Sciences*, 128, 147–160.
- Granek, J. (2016). Application of machine learning algorithms to mineral prospectivity mapping. PhD thesis, University of British Columbia, URL: <https://open.library.ubc.ca/media/stream/pdf/24/21.0340340/0340344>.
- Hronsky, J. M., & Kreuzer, O. P. (2019). Applying spatial prospectivity mapping to exploration targeting, fundamental practical issues and suggested solutions for the future. *Ore Geology Reviews*, 107, 647–653.
- Ioffe, S., & Szegedy, C. (2015). Batch normalization, accelerating deep network training by reducing internal covariate shift. International Conference on International Conference on Machine Learning. JMLR.org.
- Jiang, L., Li, C., Cai, Z., & Zhang, H. (2013). Sampled Bayesian network classifiers for class-imbalance and cost-sensitive learning. Paper presented at the 2013 IEEE 25th International Conference on Tools with Artificial Intelligence.
- Jin, W. J., Zhang, Q., He, D. F., & Jia, X. Q. (2005). SHRIMP dating of adakites in western Qinling and their implications. *Acta Petrol. Sin.*, 21, 959–966. (**In Chinese with English abstract**).
- Jin, X. Y., Li, J. W., Hofstra, A. H., & Sui, J. X. (2016). Magmatic-hydrothermal origin of the early Triassic laodou lode gold deposit in the Xiahe-Hezuo district, West Qinling orogen, china: implications for gold metallogeny. *Mineralium Deposita*, 52(6), 883–902.
- Joly, A., Porwal, A., McCuaig, T. C., Chudasama, B., Dentith, M. C., & Aitken, A. R. A. (2015). Mineral systems approach applied to GIS-based 2D-prospectivity modelling of geological regions, Insights from Western Australia. *Ore Geology Reviews*, 71, 673–702.
- Lecun, Y., Bengio, Y., & Hinton, G. (2015). Deep learning. *Nature*, 521(7553), 436–444.
- Lecun, Y., Boser, B. E., Denker, J. S., Henderson, D., & Jackel, L. D. (1990). Handwritten digit recognition with a back-propagation network. *Advances in neural information processing systems*, 2, 396–404.
- Leite, E. P., & Filho, C. R. D. S. (2009). Probabilistic neural networks applied to mineral potential mapping for platinum group elements in the Serra Leste region, Carajás Mineral Province, Brazil. *Computers & Geosciences*, 35(3), 675–687.
- Li, J. W., Sui, J. X., Jin, X. Y., Wen, G., Chang, J., Zhu, R., et al. (2019a). The intrusion-related gold deposits in the Xiahe-Hezuo district, West Qinling Orogen, Geodynamic setting and exploration potential. *Earth Science Frontiers*, 26(5), 017–032. (**In Chinese with English abstract**).
- Li, H., Li, X., Yuan, F., Jowitt, S. M., Zhang, M., Zhou, J., & Wu, B. (2020a). Convolutional neural network and transfer learning based mineral prospectivity modeling for geochemical exploration of Au mineralization within the Guandian-Zhangbalang area, Anhui Province, China. *Applied Geochemistry*, 122, 104747.
- Li, J., Sui, J., Jin, X., Wen, G., & Chang, J. (2014). A magmatic related gold system in the Xiahe-Hezuo district, Western Qinling Orogen, China. *Acta Geologica Sinica-English Edition*, 88(s2), 751–752.
- Li, J., Yuan, Z. H., Li, Z., Ren, A., Ding, C. W., Draper, J., et al. (2019b). Normalization and dropout for stochastic computing-based deep convolutional neural networks. *Integration-the Vlsi Journal*, 65, 395–403.
- Li, T., Zuo, R., Xiong, Y., & Peng, Y. (2020b). Random-drop data augmentation of deep convolutional neural network for mineral prospectivity mapping. *Natural Resources Research*. <https://doi.org/10.1007/s11053-020-09742-z>.
- Li, X. W., Mo, X. X., Yu, X. H., Ding, Y., Huang, X. F., Wei, P., et al. (2013). Petrology and geochemistry of the early Mesozoic pyroxene andesites in the Maixiu Area, West Qinling, China, Products of subduction or syn-collision? *Lithos*, 172, 158–174.
- Lin, M., Chen, Q., & Yan, S. (2013). Network in network. arXiv preprint [arXiv:1312.4400](https://arxiv.org/abs/1312.4400).
- Lindsay, M., Aitken, A., Ford, A., Dentith, M., Hollis, J., & Tyler, I. (2016). Reducing subjectivity in multi-commodity mineral prospectivity analyses, Modelling the west Kimberley, Australia. *Ore Geology Reviews*, 76, 395–413.
- Liu, Y., Zhou, K., Zhang, N., & Wang, J. (2018). Maximum entropy modeling for orogenic gold prospectivity mapping in the Tangbale-Hatu belt, western Junggar, China. *Ore Geology Reviews*, 100, 133–147.
- Lu, X., Zheng, X., & Yuan, Y. (2017). Remote sensing scene classification by unsupervised representation learning. *IEEE Transactions on Geoscience and Remote Sensing*, 9(55), 5148–5157.
- Lu, Z. Y., Nicklaw, C., Fleetwood, D., Schrimpf, R., & Pantelides, S. (2003). Erratum, structure, properties, and dynamics of oxygen vacancies in amorphous SiO₂. *Physical Review Letters*, 91(3), 039901.
- Luo, B., Zhang, H., & Lü, X. (2012a). U-Pb zircon dating, geochemical and Sr-Nd-Hf isotopic compositions of early Indosian intrusive rocks in west qinling, central china, petrogenesis and tectonic implications. *Contributions to Mineralogy & Petrology*, 164(4), 551–569.
- Luo, B. J., Zhang, H. F., & Xiao, Z. Q. (2012b). Petrogenesis and tectonic implications of the Early Indosian Meiwu pluton in

Data-driven Mineral Prospectivity

- west Qinling, central China. *Earth Science Frontiers*, 19, 199–213.
- Marmanis, D., Datcu, M., Esch, T., & Stilla, U. (2016). Deep learning earth observation classification using imangenet pre-trained networks. *IEEE Geoscience and Remote Sensing Letters*, 13(1), 105–109.
- Moeini, H., & Torab, F. M. (2017). Comparing compositional multivariate outliers with autoencoder networks in anomaly detection at Hamich exploration area, east of Iran. *Journal of Geochemical Exploration*, 180, 15–23.
- Ngiam, J., Chen, Z., Chia, D., Koh, P. W., Le, Q. V., & Ng, A. Y. (2010). Tiled convolutional neural networks. *Advances in neural information processing systems*, 23, 1279–1287.
- Nielsen, M. A. (2015). Neural networks and deep learning. Determination Press.
- Occhipinti, S. A., Metelka, V., Lindsay, M. D., Hollis, J. A., Aitken, A. R., Tyler, I. M., & McCuaig, T. C. (2016). Multicommodity mineral systems analysis highlighting mineral prospectivity in the Halls Creek Orogen. *Ore Geology Reviews*, 72, 86–113.
- Prado, E. M. G., de Souza Filho, C. R., Carranza, E. J. M., & Motta, J. G. (2020). Modeling of Cu-Au prospectivity in the carajás mineral province (Brazil) through machine learning, dealing with imbalanced training data. *Ore Geology Reviews*, 124, 103611.
- Quinlan, J. R. (1991). Improved estimates for the accuracy of small disjuncts. *Machine learning*, 6(1), 93–98.
- Ravi, D., Wong, C., Deligianni, F., Berthelot, M., Andreu-Perez, J., Lo, B., et al. (2017). Deep learning for health informatics. *IEEE Journal of Biomedical & Health Informatics*, 21(1), 4–21.
- Rodríguez-Galiano, V., Sanchez-Castillo, M., Chica-Olmo, M., & Chica-Rivas, M. (2015). Machine learning predictive models for mineral prospectivity, an evaluation of neural networks, random forest, regression trees and support vector machines. *Ore Geology Reviews*, 71, 804–818.
- Sankar, M., Batri, K., & Partvathi, R. (2016). Earliest diabetic retinopathy classification using deep convolution neural networks. *International Journal of Advanced Engineering Technology*, 2(1), 460–470.
- Shabankareh, M., & Hezarkhani, A. (2017). Application of support vector machines for copper potential mapping in Kerman region Iran. *Journal of African Earth Sciences*, 128, 116–126.
- Srivastava, N., Hinton, G., Krizhevsky, A., Sutskever, I., & Salakhutdinov, R. (2014). Dropout, a simple way to prevent neural networks from overfitting. *Journal of Machine Learning Research*, 15(1), 1929–1958.
- Stensgaard, B. M., Chung, C. J., Rasmussen, T. M., & Stendal, H. (2006). Assessment of mineral potential using cross-validation techniques and statistical analysis, a case study from the Paleoproterozoic of West Greenland. *Economic Geology*, 101(7), 1397–1413.
- Sui, J. X., Li, J. W., Wen, G., & Jin, X. Y. (2017a). The Dewulu reduced Au-Cu skarn deposit in the Xiahe-Hezuo district, West Qinling orogen, China: implications for an intrusion-related gold system. *Ore Geology Reviews*, 80, 1230–1244.
- Sui, J. X. (2012). Geochronology and genesis of the Zaozigou gold deposit, Gansu province, China. M.Sc. dissertation, China University of Geosciences, Wuhan, China (In Chinese with English abstract).
- Sui, J. X., Li, J. W., Wen, G., & Jin, X. Y. (2017b). The Dewulu reduced Au-Cu skarn deposit in the Xiahe-Hezuo district, West Qinling orogen, China, Implications for an intrusion-related gold system. *Ore Geology Reviews*, 80, 1230–1244.
- Szegedy, C., Liu, W., Jia, Y., Sermanet, P., Reed, S., Anguelov, D., Rabinovich, A. (2015). Going deeper with convolutions. In *Proceedings of the IEEE conference on computer vision and pattern recognition* (pp. 1–9).
- Torppa, J., Nykänen, V., & Molnár, F. (2019). Unsupervised clustering and empirical fuzzy memberships for mineral prospectivity modelling. *Ore Geology Reviews*, 107, 58–71.
- Vishnu, H., V. Robert, B. Kalyan., & M. Chitre. (2018). A semi-supervised learning approach to polymetallic nodule parameter modeling. OCEANS 2018 MTS/IEEE Charleston, IEEE.
- Wang, J., Zuo, R., & Xiong, Y. (2020). Mapping mineral prospectivity via semi-supervised random forest. *Natural Resources Research*, 29(1), 189–202.
- Wason, R. (2018). Deep learning, Evolution and expansion. *Cognitive Systems Research*, 52, 701–708.
- Wu, H., & Zhao, J. S. (2018). Deep convolutional neural network model based chemical process fault diagnosis. *Computers & Chemical Engineering*, 115, 185–197.
- Xiong, Y., & Zuo, R. (2016). Recognition of geochemical anomalies using a deep autoencoder network. *Computers & Geosciences*, 86, 75–82.
- Xiong, Y., Zuo, R., & Carranza, E. J. M. (2018). Mapping mineral prospectivity through big data analytics and a deep learning algorithm. *Ore Geology Reviews*, 102, 811–817.
- Yu, F., & Koltun, V. (2015). Multi-scale context aggregation by dilated convolutions. (pp. 1–13).
- Zadrożny, B., Langford, J., & Abe, N. (2003). Cost-sensitive learning by cost-proportionate example weighting. Paper presented at the Third IEEE international conference on data mining.
- Zhang, H. F., Jin, L. L., Zhang, L., Harris, N., Zhou, L., Hu, S. H., & Zhang, B. R. (2007). Geochemical and Pb-Sr-Nd isotopic compositions of granitoids from western Qinling belt, constraints on basement nature and tectonic affinity. *Sci. China Earth*, 50, 184–196.
- Zhang, S., Xiao, K., Carranza, E. J. M., Yang, F., & Zhao, Z. (2019a). Integration of auto-encoder network with density-based spatial clustering for geochemical anomaly detection for mineral exploration. *Computers & Geosciences*, 130, 43–56.
- Zhang, S., Xiao, K., Carranza, E. J. M., & Yang, F. (2019b). Maximum entropy and random forest modeling of mineral potential, analysis of gold prospectivity in the Hezuo-Meiwu District, West Qinling Orogen China. *Natural Resources Research*, 28(3), 645–664.
- Zuo, R., Xiong, Y. H., & Y. H., J. Wang, J., & Carranza E. J. M. . (2019). Deep learning and its application in geochemical mapping. *Earth-Science Reviews*, 192, 1–14.